Floquet engineering of the non-Hermitian skin effect in photonic waveguide arrays

Shaolin Ke,[1] Wanting Wen,[1] Dong Zhao,[2,*] and Yang Wang[2,†]

[1]*Hubei Key Laboratory of Optical Information and Pattern Recognition, Wuhan Institute of Technology, Wuhan 430205, China*

[2]*School of Electronic and Information Engineering, Hubei University of Science and Technology, Xianning 437100, China*

(Received 20 March 2023; accepted 26 April 2023; published 11 May 2023)

The non-Hermitian skin effect (NHSE), which involves an extensive number of bulk modes collapsing to open boundaries as skin modes, unveils a variety of unprecedented topological physics. However, achieving this effect in photonic waveguides has been challenging due to the difficulty of establishing the required non-Hermitian asymmetric couplings. Here, we investigate NHSE in photonic waveguide arrays via Floquet engineering. By periodically driving the waveguides along the propagation direction, we create an artificial gauge field (AGF) that interacts with on-site dissipation, yielding non-Hermitian asymmetric coupling and eventually giving rise to NHSE. The localization direction of NHSE is tunable by AGFs and can be detected from light propagation. In particular, we explore the interplay between NHSE and dynamical localization, whereby NHSE is suppressed by dynamical localization due to the collapse of quasienergies. Our proposed method can be extended to explore the non-Bloch Su-Schrieffer–Heeger model, with potential implications for steering light transport with the aid of NHSE.

DOI: 10.1103/PhysRevA.107.053508

I. INTRODUCTION

Topology has emerged as a new degree of freedom for manipulating the behavior of light, and has been adopted for designing advanced photonic devices that are robust against fabrication imperfections and disorders [1–8]. Recently, non-Hermitian photonic systems involving gain and loss have attracted increasing research attention due to their potential to reveal unprecedented topological physics stemming from complex eigenvalues and nonorthogonal eigenmodes [9]. Gain and loss can be introduced in photonic experiments via various means, such as optical or electric pumping, lossy material, or radiation loss. Various photonic platforms, such as waveguides [10–15], ring resonators [16,17], photonic crystals [7], metamaterials [18], and synthetic dimensions [19–22] have been used to test non-Hermitian topological physics, leading to new functionalities for photonic devices such as topological mode conversion [23–25], reconfigurable topological paths [26], and topological lasers [27–29].

Non-Hermitian Hamiltonians exhibit unique point-gap topology resulting from the nontrivial spectral winding number of eigenvalues [30–36]. If the eigenvalues in the complex plane under periodic boundary condition (PBC) enclose any nonzero areas, the non-Hermitian skin effect (NHSE) occurs under the open boundary condition (OBC), with an extensive number of bulk modes accumulated at system boundaries as skin modes [37]. A typical example of NHSE is the Hatano-Nelson model, featuring a lattice with asymmetric coupling, which leads to the unidirectional amplification of wave functions and the accumulation of bulk modes at boundaries [38,39]. The skin modes dramatically modify the conventional bulk-boundary correspondence for topological boundary modes [40]. Subsequently, biorthogonal polarization [41] and non-Bloch band theory [42] have been developed to solve this problem. NHSE also gives rise to intriguing phenomena not reveled in Hermitian systems, such as size-dependent phase transition [43,44], hybrid skin-topological modes [45,46], anomalous single-mode lasing [47], and abnormal wave dynamics [48,49]. Since NHSE has a great impact on controlling wave packets and their dynamics, it has been theoretically and experimentally demonstrated in optical fiber loops [50], ring resonators [51–58], photonic crystals [59–61], exciton polaritons [62,63], electric circuits [64], active particles [65], quantum walks [66,67], cold atoms [68,69], and mechanical lattices [70,71]. However, NHSE has not been well explored in photonic waveguide arrays mainly because the coupling coefficients between adjacent waveguides are generally Hermitian and symmetric, making it challenging to introduce the required non-Hermitian asymmetric couplings.

In this work, we theoretically propose NHSE in dissipative photonic waveguide arrays via Floquet engineering. The Floquet modulation is applied by periodically driving the propagation constants of each waveguide to arouse artificial gauge fields (AGFs) in each plaquette. The interaction of AGFs and on-site dissipation results in non-Hermitian and asymmetric coupling coefficients. Subsequently, the method is adopted to construct both Hatano-Nelson and Su-Schrieffer–Heeger (SSH) models with NHSE. We show that the localization of skin modes is tunable by AGFs, which can be directly observed through wave propagations. In addition, the Floquet waveguides experience another kind of localization known as dynamical localization, where the diffraction of light is suppressed due to the coherent destruction of tunneling at specific amplitude-to-frequency ratios [72,73]. At

*hbust_zd@163.com

†wangyang@hbust.edu.cn

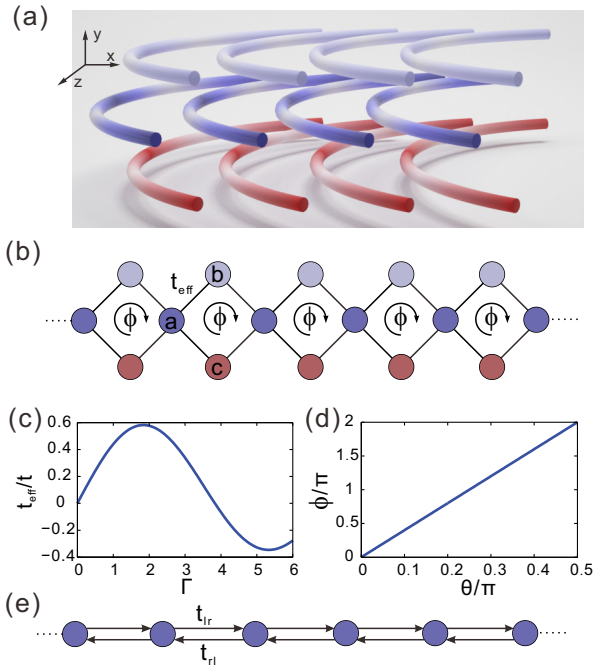

FIG. 1. Geometry and effective tight-binding lattice of proposed photonic Floquet waveguide arrays. (a) Schematic of the waveguide arrays. (b) The effective tight-binding lattice under rapid oscillating approximation. (c) The effective coupling versus amplitude-to-frequency ratio $\Gamma = A/\omega$ with A and ω denoting modulation amplitude and spatial modulation frequency, respectively. (d) The flux of AGFs as a function of modulation phase θ for $t = 1$ and $\omega = 30$. (e) The effective lattice after adiabatically eliminating sites b and c, which is a Hatano-Nelson lattice.

these specific points, the localization caused by dynamical localization dominates over NHSE. Our proposed approach offers a photonic platform for investigating NHSE and the interplay between different localization mechanisms.

II. NON-HERMITIAN ASYMMETRIC COUPLING VIA FLOQUET ENGINEERING

Figure 1(a) schematically shows the diagram of the proposed Floquet waveguide array, which is arranged in a rhombic lattice with each unit cell composed of three waveguides. The array is periodically driven along the propagation direction and bent along the x axis to create a linear gradient potential. The driving protocol is to arouse nonzero Aharonov-Bohm gauge fields in each plaquette, as previously demonstrated [74,75]. We assume weak coupling between adjacent waveguides and only consider nearest-neighbor coupling. The evolution of light is governed by the following equation,

$$\begin{aligned} -i\frac{da_n}{dz} &= t(b_n + b_{n-1} + c_n + c_{n-1}) + V_n(z)a_n, \\ -i\frac{db_n}{dz} &= t(a_n + a_{n+1}) + W_n(z)b_n + \delta_b b_n, \\ -i\frac{dc_n}{dz} &= t(a_n + a_{n+1}) + X_n(z)c_n + \delta_c c_n, \end{aligned} \tag{1}$$

where a_n, b_n, and c_n denote the amplitudes of waves at the respective waveguides in the nth cell; t stands for the original coupling coefficient; $V_n(z)$, $W_n(z)$, and $X_n(z)$ signify the periodic driving of propagation constants along the z direction; δ_b and δ_c are the additional offset of waveguides b and c. To clearly reveal AGFs produced by modulation, one can perform a gauge transformation:

$$\begin{aligned} a_n &= A_n \exp\left[-i\int_0^z V_n(z')dz'\right], \\ b_n &= B_n \exp\left[-i\int_0^t W_n(z')dz'\right], \\ c_n &= C_n \exp\left[-i\int_0^t X_n(z')dz'\right]. \end{aligned} \tag{2}$$

Substituting Eq. (2) into Eq. (1), we arrive at

$$\begin{aligned} -id\frac{A_n}{dz} &= t(e^{i\varphi_1}B_n + e^{i\varphi_2}B_{n-1} + e^{i\varphi_3}C_n + e^{i\varphi_4}C_{n-1}), \\ -i\frac{dB_n}{dz} &= t(e^{-i\varphi_1}A_n + e^{-i\varphi_2}A_{n+1}) + \delta_b B_n, \\ -i\frac{dC_n}{dz} &= t(e^{-i\varphi_3}A_n + e^{-i\varphi_4}A_{n+1}) + \delta_c C_n, \end{aligned} \tag{3}$$

with phase terms given by

$$\begin{aligned} \varphi_1 &= \int_0^z [V_n - W_n]dz', \\ \varphi_2 &= \int_0^z [V_n - W_{n-1}]dz', \\ \varphi_3 &= \int_0^z [V_n(z') - X_n(z')]dz' \\ \varphi_4 &= \int_0^z [V_n(z') - X_{n-1}(z')]dz'. \end{aligned} \tag{4}$$

The proposal aims to realize arbitrary fluxes of AGFs in each plaquette, which requires strategically setting suitable values for V_n, W_n, and X_n. To accomplish this, we slightly perturb the propagation constants of waveguides b and c along propagation direction z with a sinusoidal modulation, and introduce a linear gradient of propagation constant into each waveguide along the x direction. Specifically, we have normalized propagation distance,

$$\begin{aligned} V_n(z) &= \beta_0 - 2n\sigma, \\ W_n(z) &= \beta_0 - (2n+1)\sigma + A\cos(\omega z + \theta), \\ X_n(z) &= \beta_0 - (2n+1)\sigma - A\cos(\omega z - \theta), \end{aligned} \tag{5}$$

with β_0 denoting the basic propagation constants of each waveguide. The gradient σ along the x direction is assumed to be large ($\sigma \gg t$), and it is introduced by circularly bending waveguides along the x axis. It is related to the bending radius R as $\sigma = n_0 a/(4\pi R\lambda)$, where n_0, a, and λ are the average refractive index of the substrate, waveguide-to-waveguide separation, and incident wavelength [74]. The terms A, ω, and θ denote the amplitude, frequency, and initial phase of sinusoidal modulation, respectively, with the waveguides in the upper and lower rows undergoing opposite modulation phases. When under a resonant condition ($\sigma = M\omega$, $M \in Z$),

the coupling process between adjacent waveguides is restored. In the high-frequency limit ($\omega \gg t$), the equivalent coupling coefficients in Eq. (3) can be calculated using their cycle-averaged terms with the lowest-order approximation [75]. The resulting coupled mode equation is given as

$$\begin{aligned} -i\frac{dA_n}{dz} &= c_{\text{eff}}(e^{i\phi_1}B_n + e^{i\phi_2}B_{n-1} + e^{-i\phi_1}C_n + e^{-i\phi_2}C_{n-1}), \\ -i\frac{dB_n}{dz} &= c_{\text{eff}}(e^{-i\phi_1}A_n + e^{-i\phi_2}A_{n+1}) + \delta_b B_n, \\ -i\frac{dC_n}{dz} &= c_{\text{eff}}(e^{i\phi_1}A_n + e^{i\phi_2}A_{n+1}) + \delta_c C_n, \end{aligned} \tag{6}$$

with

$$\begin{aligned} c_{\text{eff}} &= tJ_M(\Gamma), \quad \phi_1 = -M\theta + \Gamma\sin\theta, \\ \phi_2 &= M(\pi+\theta) + \Gamma\sin\theta. \end{aligned} \tag{7}$$

The coefficient J_m signifies the Mth-order Bessel function of the first kind and $\Gamma = A/\omega$ is the amplitude-to-frequency ratio. The effective lattice is schematically illustrated in Fig. 1(b) with coupling c_{eff} and an AGF with flux $\phi = 2(\phi_1 - \phi_2) = -4M\theta$ per plaquette. The effective coupling is a Bessel function of normalized modulation amplitude and the AGF is linearly dependent of phase θ, as depicted in Figs. 1(c) and 1(d), respectively. The Hermitian part of the method to arouse AGF was theoretically proposed before and more details about the derivation can be found in [75].

The interaction between AGF and on-site dissipation yields non-Hermitian asymmetric coupling, which arises from interference from different coupling channels with different losses [34]. More specifically, light coupling from site A_n to A_{n+1} can occur through two paths via site B_n or C_n. We set the on-site offset of waveguides b and c as $\delta_b = \delta + i\gamma$ and $\delta_c = -\delta + i\gamma$, where the real part is opposite and the imaginary part is the same. The imaginary part represents the propagation loss of light waves. To gain further insight into its impact, we express the offset in the form $\delta_b = c_0 e^{i\theta_l}$, $\delta_c = -c_0 e^{-i\theta_l}$ with $\theta_l = \arctan(\gamma/\delta)$. When the offset greatly exceeds the coupling ($|\delta_b|, |\delta_c| \gg c_{\text{eff}}$), the sites B and C can be adiabatically eliminated. In this case, Eq. (6) reduces to

$$-i\frac{dA_n}{dz} = \Delta A_n + t_{rl}A_{n+1} + t_{lr}A_{n-1}, \tag{8}$$

with

$$\begin{aligned} t_{lr} &= -\frac{c_{\text{eff}}^2}{c_0}(-e^{i\phi}e^{-i\theta_l} + e^{i\theta_l}), \\ t_{rl} &= -\frac{c_{\text{eff}}^2}{c_0}(-e^{-i\phi}e^{-i\theta_l} + e^{i\theta_l}), \quad \Delta = \frac{4ic_{\text{eff}}^2}{c_0}\sin\theta_l, \end{aligned} \tag{9}$$

where t_{lr} and t_{rl} denote the forward and backward couplings between A_n and A_{n+1} and Δ is the on-site detuning. The diagram of the effective lattice after adiabatic elimination is shown in Fig. 1(e), which is a version of the Hatano-Nelson model. The coupling includes two components, which can be regarded as the summation of two interference paths via sites B and C. The effective couplings are generally asymmetric as the difference of their squared absolute value reads as

$$|t_{lr}|^2 - |t_{rl}|^2 = -\frac{4c_{\text{eff}}^4}{c_0^2}\sin(2\theta_l)\sin\phi. \tag{10}$$

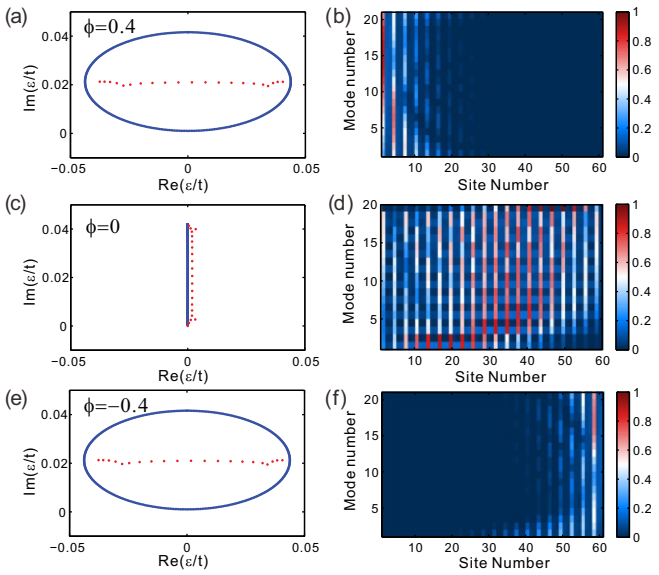

FIG. 2. NHSE in Hatano-Nelson waveguide lattice (a), (b) are the spectra of quasienergy and distribution of eigenmodes for $\phi = 0$, respectively. (c), (d) are the same as (a), (b) but for $\phi = 0.4$. (e), (f) are for $\phi = -0.4$. Other parameters are $\Gamma = 1.37$, $t = 1$, $\omega = 30$, $\delta_b = 5 + 0.5i$, and $\delta_c = -5 + 0.5$i.

The difference is not vanished as if the phase lag $\theta_l \neq m\pi/2$ and the flux of AGFs $\phi \neq m\pi$. However, in the absence of on-site dissipation, we have $\theta_l = 0$ and thus the coupling is Hermitian as $t_{lr} = t_{rl}^*$. The presence of loss and AGFs yields non-Hermitian asymmetric coupling with $|t_{lr}| \neq |t_{rl}|$. Therefore, one can expect NHSE would be realized in the proposed waveguide arrays. Experimentally, the proposal may be implemented based on the femtosecond writing technique. AGFs in waveguide arrays were reported in [74]. Our proposal requires two additional conditions, including the detuning of propagation constants and the loss in the waveguides. The detuning of propagation constants can be controlled by translation speeds of the writing process while the loss can be introduced by scattering centers generated by a pause of the longitudinal motion during the writing process [76].

III. NON-HERMITIAN SKIN EFFECT

The Floquet waveguide array can be mapped to a version of the Hatano-Nelson model with asymmetric coupling. As an example, we plot the quasienergy spectra of Floquet waveguides under PBC (blue lines) and OBC (red dots) as flux $\phi = 0.4$ in Fig. 2(a). Other parameters are set as $t = 1$, $\Gamma = 1.37$, $\omega = 30$, $\delta = 5$, and $\gamma = 0.5$ with the corresponding effective coupling coefficient and on-site loss being $t_{rl} = 0.053 + 0.051i$, $t_{lr} = 0.064 - 0.063i$, and $\Delta = 0.0228i$, respectively. By applying Floquet theory, the exact spectrum of quasienergy ε is numerically calculated by diagonalizing the Floquet Hamiltonian [75],

$$H_{\text{eff}} \equiv (i/Z)\ln U(Z), \quad U(Z) = \exp\left[-i\int_0^Z H(z')dz'\right], \tag{11}$$

where $Z = 2\pi/\omega$ is the driving period. For convenience, the quasienergy is limited in the range $-\omega/2 < \varepsilon < \omega/2$.

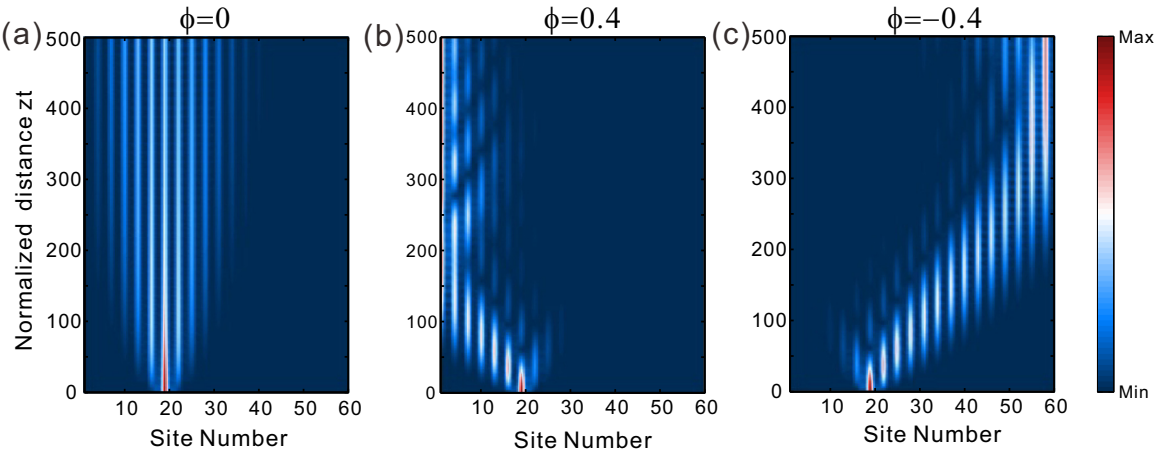

FIG. 3. Numerically calculated evolution of light to reflect NHSE for different flux. (a) The system is without skin effect as flux $\phi = 0$. (b) Left skin effect as $\phi = 0.4$. (c) Right skin effect as $\phi = -0.4$. In all cases, light is initially injected from a single site (site number $N = 19$). Other parameters are the same as those used in Fig. 2.

As shown in Fig. 2(a), the periodic spectrum forms a closed loop on the complex plane, different from that of OBC that collapses into an arc residing within the loop. According to the bulk-boundary correspondence of spectral winding, NHSE takes place under OBC as long as the periodic spectrum encloses the nonzero area [37]. The spectral winding number is intrinsic to non-Hermitian systems given by [39]

$$w = \int_{-\pi}^{\pi} \frac{dk}{2\pi} \partial_k \arg [H(k) - E_b], \tag{12}$$

where E_b is any base point. The winding number characterizes the number of times that the complex eigenenergies encircle E_b. If the spectra under PBC enclose a finite area, E_b could be chosen at the interior inside the loop, giving rise to a nonzero winding number and NHSE. The distributions of eigenmodes under OBC are illustrated Fig. 2(b), where all the modes are accumulated at the left boundary and exponentially decrease with the distance away from the boundary, clearly revealing NHSE. The skin modes undergo the strongest localization when the absolute value of t_{rl} and t_{lr} reaches the maximal difference. According to Eq. (10), it happens when the flux and phase leg of loss are $\phi = \pi/2$ and $\theta_l = \pi/2$, respectively.

In particular, the localization of skin modes can be flexibly controlled because the forward and backward couplings are related to AGFs. Figure 2(c) plots the spectra for OBC and PBC with vanished flux, with both forming open arcs on the complex plane. The spectrum under PBC has no interior, resulting in a winding number of $w = 0$, indicating that the system does not support NHSE. As illustrated in Fig. 2(d), the eigenmodes are distributed throughout the array. Furthermore, changing the sign of flux reverses the localization direction of skin modes. As indicated in Fig. 2(e), we plot the spectra for OBC and PBC as $\phi = -0.4$, which is similar to Fig. 2(a) with $\phi = 0.4$. However, all skin modes are concentrated at the right side of the array, as described in Fig. 2(f).

NHSE and its localization direction can be directly observed from wave propagation, making it a useful signature for experimental observation. In Fig. 3, we launch light from a single waveguide a with site number $n = 10$. To clearly characterize the dynamical evolution of light, the waves are normalized at each propagation distance z. In Fig. 3(a), there is no NHSE as $\phi = 0$ and the injected light broadens during the propagation. As $\phi = 0.4$, as shown in Fig. 3(b), skin modes tend to be localized at the left boundary. One can see the waves travel to the left side while they are suppressed on the right. After propagating a certain distance, light is concentrated at the left boundary, and the reflection from the boundary is suppressed. On the other hand, the direction of skin effect is reversed as $\phi = -0.4$. Light tends to propagate to the right side and accumulates at the right boundary, as shown in Fig. 3(c).

In addition to the localization stemming from NHSE, the driving waveguide arrays also experience another kind of localization known as dynamical localization [72]. Dynamical localization refers to the suppression of the broadening of wave packets arising from coherent destruction of tunneling when the charged particle interacts with ac electric fields. Sinusoidal harmonic modulation of propagation constants along the propagation direction mimics the ac field for photons, giving rising to a photonic analogy of dynamical localization at a specific amplitude-to-frequency ratio and cancellation of diffraction. More specifically, in the proposed model, the dynamical localization occurs when the amplitude-to-frequency ratio Γ takes the zero points of the Bessel function such that the effective coupling $c_{\text{eff}} = tJ_M(\Gamma) = 0$. As depicted in Fig. 1(c), the second root for vanished coupling is $\Gamma_0 \approx 3.83$ with $M = 1$. Our interest is to investigate NHSE at this point to highlight the interaction between skin modes and dynamical localization. In Fig. 4(a), we plot spectra under PBC on the complex plane for different amplitude-to-frequency ratios Γ. The periodic spectra generally form closed loops. As Γ increases, the variation of the loop area resembles the variation of the Bessel function of first order. At the zero of the J_1 function with $\Gamma_0 \approx 3.83$, the spectrum coalesces into a single point with vanished area. In the momentum space, the system should have a flat band; that is, both the real and imaginary parts of band structure $\varepsilon(k)$ are dispersionless and irrespective of momentum k. As discussed above, NHSE emerges only if the loop encloses a finite area. Therefore, NHSE will be completely suppressed at this point. Moreover, the amount of

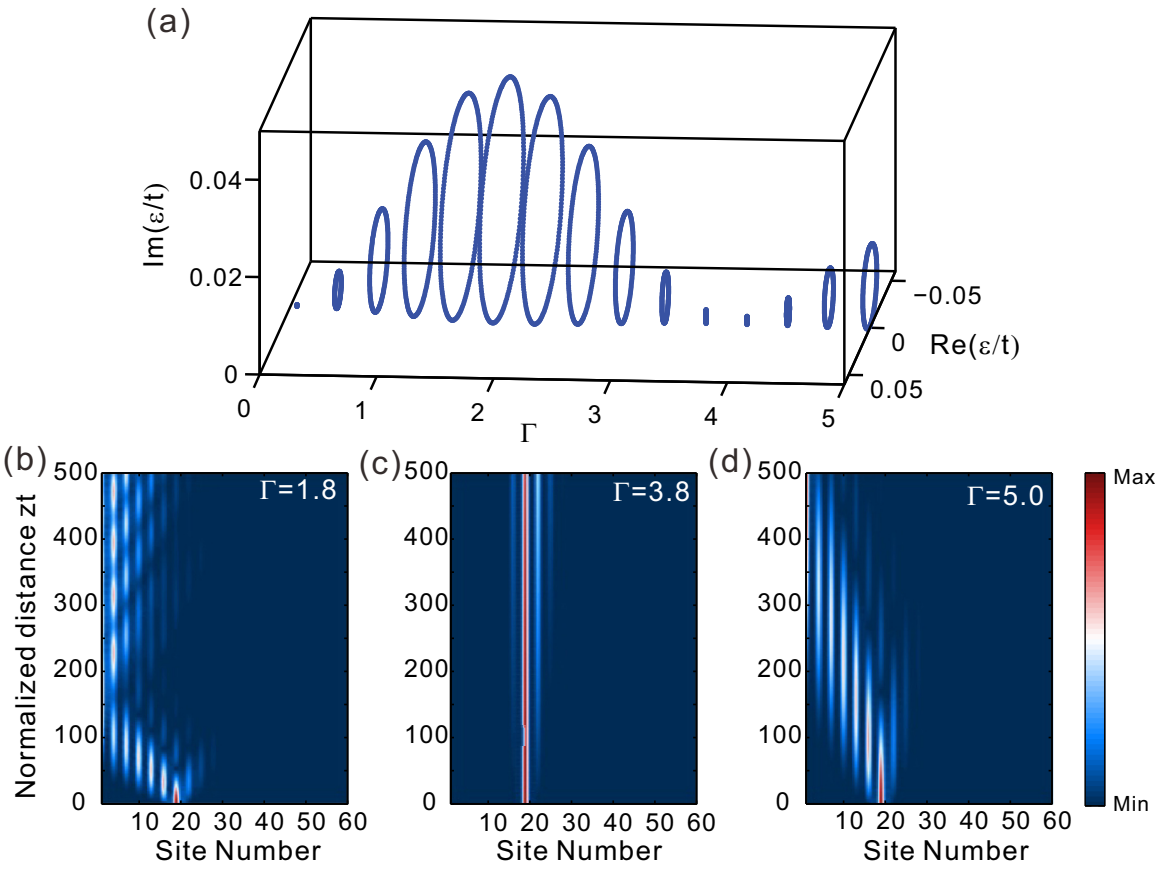

FIG. 4. The interplay of NHSE and dynamical localization. (a) The spectra under PBC for different amplitude-to-frequency ratios Γ. (b)–(d) are the evolution of light waves from single-site injection as $\Gamma = 1.8$, 3.8, and 5.0, respectively. Other parameters are the same as those used in Fig. 3(b).

loop area reflects the strength of NHSE. We could expect the strongest NHSE to appear at $\Gamma \approx 1.84$, where the function J_1 reaches its maximum.

To confirm our analysis, we numerically calculate the propagation of light waves as we launch light from a single waveguide for three different ratios with $\Gamma = 3.\ 8$, 1.8, and 5.0, as shown in Figs. 4(b)–4(d), respectively. The flux is fixed at $\phi = 0.4$, and other parameters are set as $t = 1, \omega = 30, \delta = 5, and \gamma = 0.5$. One can see that light travels to the left boundary and then is bounded to the boundary for further propagation in both Figs. 4(b) and 4(d), clearly exhibiting NHSE. In contrast, in Fig. 4(c), light is concentrated in the vicinity of the injected waveguide without broadening or traveling to the left, revealing dynamical localization in this case. The results indicate that at this point, dynamical localization dominates, leading to significant suppression of NHSE.

IV. NON-BLOCH SSH MODEL

The Floquet engineering can be adopted to construct other topological chains. As an example, we investigate the non-Bloch SSH model where the intracell coupling is non-Hermitian and asymmetric. The sectional drawing of proposed waveguides is shown in Fig. 5(a), which is composed of five waveguides in each cell labeled by a–e. The intrinsic intra- and intercouplings between adjacent waveguides are t_1 and t_2, respectively. The auxiliary waveguides b and c are periodically derived to create asymmetric intracell coupling between waveguides a and d. The intercell coupling between waveguides a and d is symmetric because there is only a single coupling channel via auxiliary waveguide e. The Floquet modulation of propagation constants in respective waveguides a–e is given by

$$\begin{aligned} V_n &= \beta_0 - 4n\sigma, \\ W_n &= \beta_0 - [4n+1]\sigma + A\cos(\omega z + \theta) + \delta_b, \\ X_n &= \beta_0 - [4n+1]\sigma - A\cos(\omega z - \theta) + \delta_c, \\ Y_n &= \beta_0 - [4n+2]\sigma, \\ Z_n &= \beta_0 - [4n+3]\sigma + A\cos(\omega z) + \delta_e. \end{aligned} \tag{13}$$

The resulting effective intracell coupling $t_{\text{eff}1} = t_1 J_M(\Gamma)$ with AGFs $\phi = 4M\theta$, and the effective intercell coupling $t_{\text{eff}2} = t_2 J_M(\Gamma)$. Assuming the additional on-site detuning of propagation constants $\delta_{b,c,e}$ greatly exceeds the coupling strength, we can adiabatically eliminate sites b, c, and e. Then a non-Bloch SSH model is achieved, as schematically shown in the lower panel of Fig. 5(a), where the forward and backward intracell couplings are labeled by t_{rl} and t_{lr} and intercell is t_{e2}.

The SSH chain is well known to sustain topological edge modes that appear at a topologically nontrivial phase. The

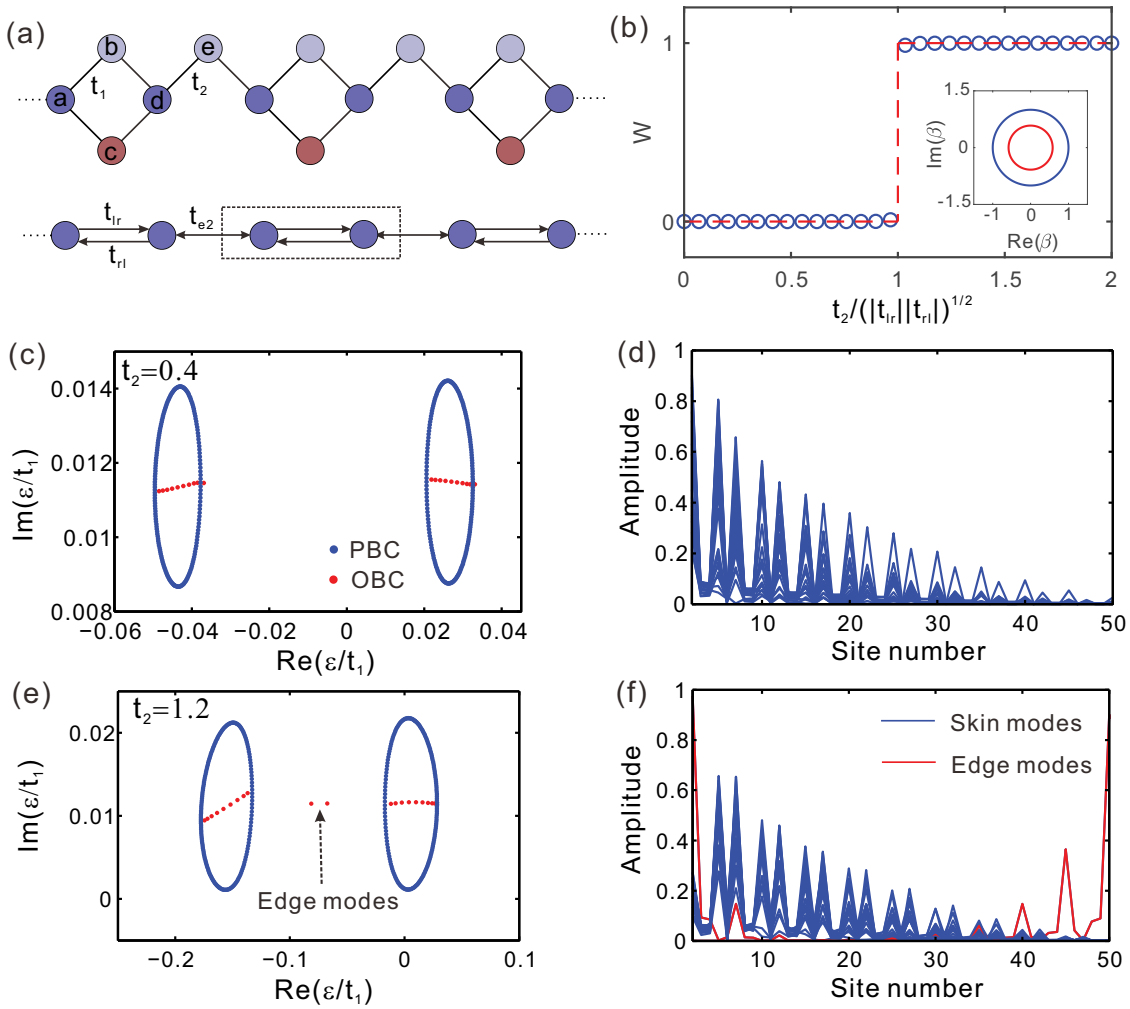

FIG. 5. The proposal of non-Bloch SSH lattice based on Floquet waveguide arrays. (a) Schematic of tight-binding lattice of SSH model. The upper and lower panels are the original lattice and the effective lattice after adiabatic elimination, respectively. (b) Non-Bloch topological invariants for SSH model. The inset depicts the GBZ. (c), (d) are the spectra and mode profiles in the topologically trivial phase with $t_2 = 0.4$. (e), (f) stand for the topologically nontrivial phase with $t_2 = 1.2$. Other parameters are $\Gamma = 1.37$, $t_1 = 1$, $\omega = 30$, $\delta_b = 5 + 0.5i$, $\delta_c = -5 + 0.5i$, and $\delta_e = 5$.

emergence of these modes is guaranteed by the bulk-boundary correspondence with the topological invariant determined by the bulk modes. For the standard SSH model, the phase transition occurs when the intra- and intercell couplings are equal. However, the bulk-boundary correspondence breaks down when the bulk modes develop into skin modes, resulting in the derivation of the phase transition. To deal with this situation, the non-Bloch topological band theory should be applied based on the generalized Brillouin zone (GBZ). GBZ is a more general case by replacing Bloch phase factor $\exp(ik)$ with a complex value α. The GBZ is determined by the characteristic equation

$$\det[H_{\mathrm{SSH}}(\alpha) - \varepsilon I] = 0, \tag{14}$$

which has two roots $\alpha_{1,2}$, satisfying $\alpha_{1,2} = |t_{rl}||t_{lr}|$. The boundary condition requires that they must have the same absolute value $|\alpha_1| = |\alpha_2|$, yielding $\alpha_1 = (t_{lr}/t_{rl})^{1/2} e^{i\varphi}$ and $\alpha_1 = (t_{lr}/t_{rl})^{1/2} e^{-i\varphi}$. Their trajectory on the complex planes forms the GBZ, which is a circle with radius $|t_{lr}|/|t_{rl}|$, as plotted in the inset of Fig. 5(b). GBZ can be also used to indicate NHSE, which is consistent with the spectral winding number. As GBZ is within (outside of) the unit circle, the skin modes are accumulated at the left (right) boundary. Furthermore, the non-Bloch topological invariant for edge modes is reconstructed in the GBZ with

$$W = \frac{i}{2\pi} \int_{C_\alpha} q^{-1} dq, \tag{15}$$

where q is the off-diagonal element of the Q matrix,

$$Q(\alpha) = |\tilde{u}_R(\alpha)\rangle\langle\tilde{u}_L(\alpha)| - |u_R(\alpha)\rangle\langle u_L(\alpha)| = \begin{pmatrix} 0 & q \\ q^{-1} & 0 \end{pmatrix}, \tag{16}$$

with $|u_R(\alpha)\rangle$ and $\langle u_L(\alpha)|$ denoting the right and left eigenvectors, and $|\tilde{u}_R(\alpha)\rangle = \sigma_z|u_R(\alpha)\rangle$, $|\tilde{u}_L(\alpha)\rangle = \sigma_z|u_L(\alpha)\rangle$. The non-Bloch winding number is plotted in Fig. 5(b), where the phase transition takes place at $t_{e2} = \mathrm{sqrt}(|t_{rl}||t_{lr}|)$.

We further numerically calculate the quasienergy spectra and eigenmodes in topologically trivial ($t_{e2} < \mathrm{sqrt}(|t_{rl}||t_{lr}|)$) and nontrivial ($t_{e2} > \mathrm{sqrt}(|t_{rl}||t_{lr}|)$) phases. The results are pre-

sented in Figs. 5(c)–5(f). In the trivial case, the spectra under PBC form two separate loops, with the spectra under OBC contained within them [Fig. 5(c)]. No edge modes exist in this case. The distribution of eigenmodes is shown in Fig. 5(d), where skin modes are localized at the left boundary. In the nontrivial phase, the periodic spectrum still forms two closed loops [Fig. 5(e)]. However, the quasienergies under OBC have two additional points outside the loop, corresponding to two topological edge modes. The distributions of eigenmodes are plotted in Fig. 5(f), with the edge modes indicated by red lines, one at the left and the other at the right. At the same time, all skin modes are concentrated at the left boundary. The topological modes may be pushed into the bulk at some critical parameters as they experience topological localization and skin effect at the same time. When the strengths of two different effects are balanced, the topological modes become extended throughout the whole structure [70,77].

V. CONCLUSIONS

In conclusion, we have proposed non-Hermitian Hatano-Nelson and SSH models in photonic waveguides based on Floquet modulation. which is achieved by periodically driving the waveguides along the propagation direction. The Floquet engineering introduces AGFs into waveguides, and their interaction with on-site dissipation successfully arouses non-Hermitian asymmetric coupling. As a result, the quasienergy spectra form closed loops on the complex plane and exhibit nontrivial spectral winding, which is accompanied with NHSE under OBC. Furthermore, the asymmetric coupling is tunable by AGFs, and hence the localization direction of skin modes can be controlled via Floquet engineering. We show NHSE is directly viewed from light propagation as the reflection of waves is suppressed at the boundary of the array. In particular, Floquet driving also mimics ac electric fields and leads to dynamical localization. When dynamical localization takes place, NHSE is suppressed as a result of the collapse of quasienergies. On the other hand, the SSH model simultaneously supports skin modes and topological edge modes, exhibiting non-Bloch bulk-boundary correspondence. The study provides a route toward investigating NHSE on a photonic platform, which can also be extended to explore other non-Hermitian topological behaviors such as high-order skin effect, hybrid skin-topological modes, and topological extended modes.

ACKNOWLEDGMENTS

The work is supported by the 14th Graduate Education Innovation Fund of Wuhan Institute of Technology (Grants No. CX2022464 and No. CX2022469), the National Natural Science Foundation of China (NSFC) (Grant No. 12274157), and the Natural Science Foundation of Hubei Province of China (Grant No. 2022CFB179).

[1] T. Ozawa, H. M. Price, A. Amo, N. Goldman, M. Hafezi, L. Lu, M. C. Rechtsman, D. Schuster, J. Simon, O. Zilberberg *et al.*, Topological photonics, Rev. Mod. Phys. **91**, 015006 (2019).

[2] H. Price, Y. Chong, A. Khanikaev, H. Schomerus, L. J Maczewsky, M. Kremer, M. Heinrich, A. Szameit, O. Zilberberg, Y. Yang *et al.*, Roadmap on topological photonics, J. Phys. Photonics **4**, 032501 (2022).

[3] R. Banerjee, S. Mandal, and T. C. H. Liew, Coupling between Exciton-Polariton Corner Modes through Edge States, Phys. Rev. Lett. **124**, 063901 (2020).

[4] C. Jiang, Y. Song, X. Li, P. Lu, and S. Ke, Photonic Möbius topological insulator from projective symmetry in multiorbital waveguides, Opt. Lett. **48**, 2337 (2023).

[5] C. Jiang, Y. Wu, M. Qin, and S. Ke, Topological bound modes with orbital angular momentum in optical waveguide arrays, J. Lightwave Technol. **41**, 2205 (2023).

[6] S. Mandal, G.-G. Liu, and B. Zhang, Topology with memory in nonlinear driven-dissipative photonic lattices, ACS Photonics **10**, 147 (2023).

[7] L. Xie, L. Jin, and Z. Song, Antihelical edge states in two-dimensional photonic topological metals, Sci. Bull. **68**, 255 (2023).

[8] R. Banerjee, S. Mandal, and T. C. H. Liew, Optically induced topological spin-valley Hall effect for exciton polaritons, Phys. Rev. B **103**, L201406 (2021).

[9] Y. Ota, K. Takata, T. Ozawa, A. Amo, Z. Jia, B. Kante, M. Notomi, Y. Arakawa, and S. Iwamoto, Active topological photonics, Nanophotonics **9**, 547 (2020).

[10] M. C. Rechtsman, J. M. Zeuner, Y. Plotnik, Y. Lumer, D. Podolsky, F. Dreisow, S. Nolte, M. Segev, and A. Szameit, Photonic Floquet topological insulators, Nature (London) **496**, 196 (2013).

[11] W. Song, W. Sun, C. Chen, Q. Song, S. Xiao, S. Zhu, and T. Li, Breakup and Recovery of Topological Zero Modes in Finite Non-Hermitian Optical Lattices, Phys. Rev. Lett. **123**, 165701 (2019).

[12] S. Weimann, M. Kremer, Y. Plotnik, Y. Lumer, S. Nolte, K. G. Makris, M. Segev, M. C. Rechtsman, and A. Szameit, Topologically protected bound states in photonic parity–time-symmetric crystals, Nat. Mater. **16**, 433 (2017).

[13] S. Ke, D. Zhao, J. Liu, Q. Liu, Q. Liao, B. Wang, and P. Lu, Topological bound modes in anti-$\mathcal{PT}$-symmetric optical waveguide arrays, Opt. Express **27**, 13858 (2019).

[14] S. Ke, D. Zhao, J. Fu, Q. Liao, B. Wang, and P. Lu, Topological edge modes in non-Hermitian photonic Aharonov-Bohm cages, IEEE J. Sel. Top. Quantum Electron. **26**, 1 (2020).

[15] S. Wu, W. Song, S. Gao, Y. Chen, S. Zhu, and T. Li, Floquet π mode engineering in non-Hermitian waveguide lattices, Phys. Rev. Res. **3**, 023211 (2021).

[16] M. Hafezi, S. Mittal, J. Fan, A. Migdall, and J. M. Taylor, Imaging topological edge states in silicon photonics, Nat. Photonics. **7**, 1001 (2013).

[17] D. Leykam and L. Yuan, Topological phases in ring resonators: Recent progress and future prospects, Nanophotonics **9**, 4473 (2020).

[18] Z. Guo, T. Zhang, J. Song, H. Jiang, and H. Chen, Sensitivity of topological edge states in a non-Hermitian dimer chain, Photonics Res. **9**, 574 (2021).

[19] C. Leefmans, A. Dutt, J. Williams, L. Yuan, M. Parto, F. Nori, S. Fan, and A. Marandi, Topological dissipation in a time-multiplexed photonic resonator network, Nat. Phys. **18**, 442 (2022).

[20] L. Zheng, B. Wang, C. Qin, L. Zhao, S. Chen, W. Liu, and P. Lu, Chiral Zener tunneling in non-Hermitian frequency lattices, Opt. Lett. **47**, 4644 (2022).

[21] Y. Song, Y. Chen, W. Xiong, and M. Wang, Flexible light manipulation in non-Hermitian frequency Su–Schrieffer–Heeger lattice, Opt. Lett. **47**, 1646 (2022).

[22] Y. Song, S. Ke, Y. Chen, and M. Wang, Mode-locking in anti-$\mathcal{PT}$ symmetric frequency lattices, Appl. Phys. Lett. **122**, 151106 (2023).

[23] J. Doppler, A. A. Mailybaev, J. Böhm, U. Kuhl, A. Girschik, F. Libisch, T. J. Milburn, P. Rabl, N. Moiseyev, and S. Rotter, Dynamically encircling an exceptional point for asymmetric mode switching, Nature (London) **537**, 76 (2016).

[24] A. Li, W. Chen, H. Wei, G. Lu, A. Alù, C.-W. Qiu, and L. Chen, Riemann-Encircling Exceptional Points for Efficient Asymmetric Polarization-Locked Devices, Phys. Rev. Lett. **129**, 127401 (2022).

[25] X.-L. Zhang, T. Jiang, and C. T. Chan, Dynamically encircling an exceptional point in anti-parity-time symmetric systems: Asymmetric mode switching for symmetry-broken modes, Light Sci. Appl. **8**, 88 (2019).

[26] H. Zhao, X. Qiao, T. Wu, B. Midya, S. Longhi, and L. Feng, Non-Hermitian topological light steering, Science **365**, 1163 (2019).

[27] M. A. Bandres, S. Wittek, G. Harari, M. Parto, J. Ren, M. Segev, D. N. Christodoulides, and M. Khajavikhan, Topological insulator laser: Experiments, Science **359**, eaar4005 (2018).

[28] P. Comaron, V. Shahnazaryan, W. Brzezicki, T. Hyart, and M. Matuszewski, Non-Hermitian topological end-mode lasing in polariton systems, Phys. Rev. Res. **2**, 022051(R) (2020).

[29] G. Salerno, R. Heilmann, K. Arjas, K. Aronen, J.-P. Martikainen, and P. Törmä, Loss-Driven Topological Transitions in Lasing, Phys. Rev. Lett. **129**, 173901 (2022).

[30] K. Kawabata, K. Shiozaki, M. Ueda, and M. Sato, Symmetry and Topology in Non-Hermitian Physics, Phys. Rev. X **9**, 041015 (2019).

[31] X. Zhang, T. Zhang, M.-H. Lu, and Y.-F. Chen, A review on non-Hermitian skin effect, Adv. Phys.: X **7**, 2109431 (2022).

[32] E. J. Bergholtz, J. C. Budich, and F. K. Kunst, Exceptional topology of non-Hermitian systems, Rev. Mod. Phys. **93**, 015005 (2021).

[33] H. Li and W. Yi, Topology and its detection in a dissipative Aharonov-Bohm chain, Phys. Rev. A **106**, 053311 (2022).

[34] X. Huang, C. Lu, C. Liang, H. Tao, and Y.-C. Liu, Loss-induced nonreciprocity, Light Sci. Appl. **10**, 30 (2021).

[35] C. Yuce and H. Ramezani, Stabilization of zero-energy skin modes in finite non-Hermitian lattices, Phys. Rev. A **106**, 063501 (2022).

[36] Y. Wu, J. Zou, C. Jiang, X. Li, and S. Ke, Direction-dependent non-Hermitian skin effect in modulated photonic waveguide arrays, Front. Phys. **10**, 1073295 (2022).

[37] K. Zhang, Z. Yang, and C. Fang, Correspondence between Winding Numbers and Skin Modes in Non-Hermitian Systems, Phys. Rev. Lett. **125**, 126402 (2020).

[38] N. Hatano and D. R. Nelson, Non-Hermitian delocalization and eigenfunctions, Phys. Rev. B **58**, 8384 (1998).

[39] Z. Gong, Y. Ashida, K. Kawabata, K. Takasan, S. Higashikawa, and M. Ueda, Topological Phases of Non-Hermitian Systems, Phys. Rev. X **8**, 031079 (2018).

[40] T. E. Lee, Anomalous Edge State in a Non-Hermitian Lattice, Phys. Rev. Lett. **116**, 133903 (2016).

[41] F. K. Kunst, E. Edvardsson, J. C. Budich, and E. J. Bergholtz, Biorthogonal Bulk-Boundary Correspondence in Non-Hermitian Systems, Phys. Rev. Lett. **121**, 026808 (2018).

[42] S. Yao and Z. Wang, Edge States and Topological Invariants of Non-Hermitian Systems, Phys. Rev. Lett. **121**, 086803 (2018).

[43] Z. B. Siu, S. M. Rafi-Ul-Islam, and M. B. A. Jalil, Critical non-Hermitian skin effect in a single closed non-Hermitian chain, doi: 10.21203/rs.3.rs-1312995/v1.

[44] L. Li, C. H. Lee, S. Mu, and J. Gong, Critical non-Hermitian skin effect, Nat. Commun. **11**, 5491 (2020).

[45] C. H. Lee, L. Li, and J. Gong, Hybrid Higher-Order Skin-Topological Modes in Nonreciprocal Systems, Phys. Rev. Lett. **123**, 016805 (2019).

[46] W. Zhu and J. Gong, Hybrid skin-topological modes without asymmetric couplings, Phys. Rev. B **106**, 035425 (2022).

[47] B. F. Zhu, Q. Wang, D. Leykam, H. R. Xue, Q. J. Wang, and Y. D. Chong, Anomalous Single-Mode Lasing Induced by Nonlinearity and the Non-Hermitian Skin Effect, Phys. Rev. Lett. **129**, 013903 (2022).

[48] H. Li and S. Wan, Dynamic skin effects of non-Hermitian systems, Phys. Rev. B **106**, L241112 (2022).

[49] S. Longhi, Non-Hermitian skin effect and self-acceleration, Phys. Rev. B **105**, 245143 (2022).

[50] S. Weidemann, M. Kremer, T. Helbig, T. Hofmann, A. Stegmaier, M. Greiter, R. Thomale, and A. Szameit, Topological funneling of light, Science **368**, 311 (2020).

[51] Y. G. N. Liu, Y. Wei, O. Hemmatyar, G. G. Pyrialakos, P. S. Jung, D. N. Christodoulides, and M. Khajavikhan, Complex skin modes in non-Hermitian coupled laser arrays, Light Sci. Appl. **11**, 336 (2022).

[52] X. Zhang, Y. Tian, J.-H. Jiang, M.-H. Lu, and Y.-F. Chen, Observation of higher-order non-Hermitian skin effect, Nat. Commun. **12**, 5377 (2021).

[53] X. Zhu, H. Wang, S. K. Gupta, H. Zhang, B. Xie, M. Lu, and Y. Chen, Photonic non-Hermitian skin effect and non-Bloch bulk-boundary correspondence, Phys. Rev. Res. **2**, 013280 (2020).

[54] S. Longhi, D. Gatti, and G. D. Valle, Robust light transport in non-Hermitian photonic lattices, Sci. Rep. **5**, 13376 (2015).

[55] Z. Gu, H. Gao, H. Xue, J. Li, Z. Su, and J. Zhu, Transient non-Hermitian skin effect, Nat. Commun. **13**, 7668 (2022).

[56] Z. Lin, L. Ding, S. Ke, and X. Li, Steering non-Hermitian skin modes by synthetic gauge fields in optical ring resonators, Opt. Lett. **46**, 3512 (2021).

[57] S.-Y. Chen, C. Jiang, S.-L. Ke, B. Wang, and P.-X. Lu, Suppression of non-Hermitian skin effect via Aharonov-Bohm cage, Acta Phys. Sin. **71**, 174201 (2022).

[58] H. Gao, H. Xue, Z. Gu, L. Li, W. Zhu, Z. Su, J. Zhu, B. Zhang, and Y. D. Chong, Anomalous Floquet non-Hermitian skin effect in a ring resonator lattice, Phys. Rev. B **106**, 134112 (2022).

[59] J. Zhong, K. Wang, Y. Park, V. Asadchy, C. C. Wojcik, A. Dutt, and S. Fan, Nontrivial point-gap topology and non-Hermitian skin effect in photonic crystals, Phys. Rev. B **104**, 125416 (2021).

[60] K. Yokomizo, T. Yoda, and S. Murakami, Non-Hermitian waves in a continuous periodic model and application to photonic crystals, Phys. Rev. Res. **4**, 023089 (2022).

[61] Z. Fang, M. Hu, L. Zhou, and K. Ding, Geometry-dependent skin effects in reciprocal photonic crystals, Nanophotonics **11**, 3447 (2022).

[62] S. Mandal, R. Banerjee, E. A. Ostrovskaya, and T. C. H. Liew, Nonreciprocal Transport of Exciton Polaritons in a Non-Hermitian Chain, Phys. Rev. Lett. **125**, 123902 (2020).

[63] S. Mandal, R. Banerjee, and T. C. H. Liew, From the topological spin-Hall effect to the non-Hermitian skin effect in an elliptical micropillar chain, ACS Photonics **9**, 527 (2022).

[64] T. Helbig, T. Hofmann, S. Imhof, M. Abdelghany, T. Kiessling, L. W. Molenkamp, C. H. Lee, A. Szameit, M. Greiter, and R. Thomale, Generalized bulk–boundary correspondence in non-Hermitian topolectrical circuits, Nat. Phys. **16**, 747 (2020).

[65] L. S. Palacios, S. Tchoumakov, M. Guix, I. Pagonabarraga, S. Sánchez, and A. G. Grushin, Guided accumulation of active particles by topological design of a second-order skin effect, Nat. Commun. **12**, 4691 (2021).

[66] K. Wang, T. Li, L. Xiao, Y. Han, W. Yi, and P. Xue, Detecting Non-Bloch Topological Invariants in Quantum Dynamics, Phys. Rev. Lett. **127**, 270602 (2021).

[67] L. Xiao, T. Deng, K. Wang, G. Zhu, Z. Wang, W. Yi, and P. Xue, Non-Hermitian bulk–boundary correspondence in quantum dynamics, Nat. Phys. **16**, 761 (2020).

[68] S. Guo, C. Dong, F. Zhang, J. Hu, and Z. Yang, Theoretical prediction of non-Hermitian skin effect in ultracold atom Systems, Phys. Rev. A **106**, L061302 (2022).

[69] Q. Liang, D. Xie, Z. Dong, H. Li, H. Li, B. Gadway, W. Yi, and B. Yan, Dynamic Signatures of Non-Hermitian Skin Effect and Topology in Ultracold Atoms, Phys. Rev. Lett. **129**, 070401 (2022).

[70] W. Wang, X. Wang, and G. Ma, Non-Hermitian morphing of topological modes, Nature (London) **608**, 50 (2022).

[71] A. Ghatak, M. Brandenbourger, J. van Wezel, and C. Coulais, Observation of non-Hermitian topology and its bulk–edge correspondence in an active mechanical metamaterial, Proc. Natl. Acad. Sci. USA **117**, 29561 (2020).

[72] S. Longhi, M. Marangoni, M. Lobino, R. Ramponi, P. Laporta, E. Cianci, and V. Foglietti, Observation of Dynamic Localization in Periodically Curved Waveguide Arrays, Phys. Rev. Lett. **96**, 243901 (2006).

[73] S. Wang *et al.*, High-order dynamic localization and tunable temporal cloaking in ac-electric-field driven synthetic lattices, Nat. Commun. **13**, 7653 (2022).

[74] S. Mukherjee, M. Di Liberto, P. Öhberg, R. R. Thomson, and N. Goldman, Experimental Observation of Aharonov-Bohm Cages in Photonic Lattices, Phys. Rev. Lett. **121**, 075502 (2018).

[75] S. Longhi, Aharonov–Bohm photonic cages in waveguide and coupled resonator lattices by synthetic magnetic fields, Opt. Lett. **39**, 5892 (2014).

[76] T. Biesenthal, M. Kremer, M. Heinrich, and A. Szameit, Experimental Realization of $\mathcal{PT}$-Symmetric Flat Bands, Phys. Rev. Lett. **123**, 183601 (2019).

[77] W. Zhu, W. X. Teo, L. Li, and J. Gong, Delocalization of topological edge states, Phys. Rev. B **103**, 195414 (2021).